This is a preprint, the final version is subject to change, of the American Mineralogist (MSA)
Cite as Authors (Year) Title. American Mineralogist, in press.
DOI: https://doi.org/10.2138/am-2018-6128

Structure of low-order hemimorphite produced in a Zn-rich environment by cyanobacterium *Leptolingbya frigida*

DANIELA MEDAS[1], CARLO MENEGHINI[2], FRANCESCA PODDA[1], COSTANTINO FLORIS[1], MARIANO CASU[1], MARIA ANTONIETTA CASU[3], ELODIA MUSU[4], GIOVANNI DE GIUDICI[1,*]

[1]Department of Chemical and Geological Sciences, University of Cagliari, S.S. 554, 09042 Monserrato, Cagliari, Italy

[2] Department of Sciences, University of Roma Tre, Via della Vasca Navale 84, 00146 Rome, Italy

[3] National Research Council, Institute of Translational Pharmacology, UOS of Cagliari, Scientific and Technological Park of Sardinia - POLARIS, 09010 Pula, Cagliari, Italy

[4] CRS4- Microlab Scientific and Technological Park of Sardinia, 09010 Pula, Cagliari, Italy

*E-mail: gbgiudic@unica.it

REVISION 3

ABSTRACT

Microbes play a fundamental role in the precipitation of silicate biominerals, thereby affecting the Si geochemical cycle. The fine mechanisms ruling biomineralization are not yet fully understood, and their microscopic structures can offer deep insight into their processes of formation, reactivity and stability. In this study, a Zn silicate biomineral, extracellularly produced by cyanobacterium *Leptolingbya frigida*, was investigated combining Nuclear Magnetic Resonance (NMR), Zn K-edge X-ray Absorption Spectroscopy (XAS) and other complementary techniques. ^{29}Si Magic Angle Spinning and ^{29}Si/^{1}H Cross Polarization Magic Angle Spinning analysis, Fourier Transform Infrared Spectroscopy (FTIR) and XAS analysis revealed a poorly crystalline phase closely resembling hemimorphite ($Zn_4Si_2O_7(OH)_2 \cdot H_2O$). Zn K-edge Extended X-ray Absorption Fine Structure (EXAFS) provided further structural details, revealing that the Zn-O-Si interatomic distances were 7%–8% shorter than the abiotic mineral. ^{13}C NMR spectra analysis was conducted to investigate the composition of the Zn silicate biomineral organic matrix, and results revealed that C atoms occurred in

several functional groups such as carbonyl carbons, C rings, O-aliphatic chains, N-aliphatic chains and aliphatic chains.

Under slightly alkaline conditions, bacterial cell walls exhibited fundamental control on the biomineralization process by binding Zn ions and forming Zn–O–Si bonds. In this way, *L. frigida* cell walls served as a reactive surface for the precipitation of this Zn sorosilicate, hindering the condensation of silicon dimers. Moreover, we found a ^{29}Si NMR band at 85 ppm that could be attributed to a $(C_3H_6O_3)_2Si$ complex. This complex could play a role in the control of silicon polymerisation, with implications for Si biomineralization processes.

Keywords: zinc, silicon, biomineral, hemimorphite, silicon polymerisation, organic Si complexes

INTRODUCTION

In geological history, several kinds of organisms have adopted biosynthesis strategies producing Si biominerals, significantly affecting the Si geochemical cycle (Konhauser, 2016). Diatoms and sponges are among the most studied silica biominerals. Diatoms produce their biominerals by polycondensation of $Si(OH)_4$ (silicic acid) molecules, which occurs in a specific intracellular compartment, termed the silica deposition vesicle (Drum and Pankratz 1964). Sponges (the Porifera) are multicellular (differentiated) sedentary filter-feeder organisms that can produce intracellularly silicified spicules in specialised cells known as sclerocytes (reviewed in Simpson 1984). Other silicifying systems use silica to build biominerals of specific shape and crystal order. Silica and silicates can be found in many higher plants and occur in cell walls, cell lumens, intracellular spaces, roots, leaves and other spaces (Ma et al. 2001; Neumann and zur Nieden 2001; Valtchev et al. 2003; Ma and Yamaji 2008; Schaller et al. 2013; De Giudici et al. 2014a and 2015; Medas et al. 2015).

Biosilicification mechanisms mediated by bacteria, either involving metal precipitation or not, were extensively investigated in geothermal waters oversaturated with respect to SiO_{2am} (Köhler et al. 1994; Fortin et al. 1998; Phoenix et al. 2000). In these systems, silica sinter formation (Benning et al. 2005) is interpreted as a multi-step process: thermodynamically driven polycondensation of silica monomers and the formation of silica

nanoparticles first take place, followed by microbially enhanced aggregation of the silica nanostructures into large assemblages. However, little research has been performed on biosilicates precipitated by bacteria from waters undersaturated with SiO_{2am}, and the control that biopolymers have on Si coordination during biosynthesis is only partially understood. Previous studies pointed out that Fe and/or Al hydroxide-coated cyanobacteria can bind a significant concentration of Si, thereby suggesting that Mg, Fe and Al play an important role in the formation of silicate biominerals (Urrutia and Beveridge 1993; Konhauser 1998; Konhauser et al. 1993; Fein et al. 2002; Zeyen et al. 2015). In some actual alkaline lakes (Burne et al. 2014; Zeyen et al. 2015, and references therein) with waters undersaturated in silica, cyanobacteria drive the precipitation of Mg–silicate, stevensite ($(Ca_{0.09}K_{0.01}Sr_{0.01})_{\Sigma=0.11}$ $(Mg_{2.84}Fe_{0.02}Al_{0.03})_{\Sigma=2.89}(Si_{3.98}Al_{0.02}O_{10})$ $(OH)_2 \cdot nH_2O$) or kerolite ($Mg_3Si_4O_{10}(OH)_2 \cdot nH_2O$), two talc-like phases, which form a matrix rich in biopolymers, onto which aragonite precipitates. The same authigenic Mg silicate was also found by Zeyen et al. (2015) in modern microbialites from alkaline crater lakes, suggesting that biopolymers can influence ageing of minerals. Zeyen et al. (2015) left open the question if the process is driven by template, metabolic effect or a mixture of them. Nevertheless, a better understanding of the processes driving the formation of these Mg silicate biominerals can explain a missing link for microbialite formation.

Podda et al. (2014) found that a cyanobacterium, identified by molecular biology as *Leptolyngbya frigida*, at Rio Naracauli (SW Sardinia, Italy) is able to produce an amorphous Zn silicate phase coating the cell wall of the cyanobacteria, likely due to a dominant extracellular mechanism (Wanty et al. 2013). High-quality Synchrotron radiation X-ray diffraction patterns of the Zn silicate (Medas et al. 2014b) are characterised by a broad halo, which indicates an amorphous-like phase. Zn K-edge X-ray Absorption Spectroscopy (XAS) analysis proved that this biomineral can be considered a precursor of hemimorphite ($Zn_4Si_2O_7(OH)_2 \cdot H_2O$) that we describe as bio-hemimorphite. In this work, a deep understanding of the coordinative environment and chemical bonding of Si, Zn and C in this extracellularly biosynthesised Zn-rich phase is obtained by combining electron microscopy, Fourier Transform Infrared Spectroscopy (FTIR), (Nuclear Magnetic Resonance (NMR) and XAS techniques.

MATERIALS AND METHODS

Samples for this study included natural biomineral samples from Rio Naracauli (labelled WM, 'white mud', because they were first described with this term; Fig. S1), as well as crystalline, supposedly abiotic, hemimorphite and hydrozincite ($Zn_5(CO_3)_2(OH)_6$) from San Giovanni Mine and Malfidano Mine, Sardinia (Italy), respectively. Biomineral samples were collected between summer 1995 and summer 2010. In a previous work (Medas et al. 2014b), we proved through X-ray diffraction analysis that bio-hemimorphite sampled along Rio Naracauli is mainly amorphous (representative X-ray diffraction patterns of the investigated samples are reported in Fig. S2), except for few weak diffraction peaks of quartz occurring as accessory mineral. XRD patterns of abiotic hemimorphite were also reported (SM, Fig. S2) for comparison (for further details, see Medas et al. 2014b; Podda et al. 2014; De Giudici et al. 2014b).

Scanning Electron Microscopy (SEM) imaging and energy dispersive spectroscopy analysis were carried out using an environmental scanning electron microscope (ESEM QUANTA 200, FEI) and a field emission (Schottky thermal field emitter) SEM under high vacuum conditions. To obtain better quality images, samples were gold coated before observation using a SEM Coating Unit PS3 (Agar Aids for Electron Microscopy).

Thin sections (90 nm) of the biomineral samples were cut with a diamond knife on ultramicrotome and collected on carbon-coated copper grids, which were dried at room temperature. For details on sample preparation, see Medas et al. 2014b. Sections were then analysed by bright-field Transmission Electron Microscopy (TEM) on a FEI Tecnai 12 TEM operating at an accelerating voltage of 120 kV.

FTIR spectra were collected in the middle region from 400 cm^{-1} to 4000 cm^{-1} at a 4 cm^{-1} resolution over 64 averaged scans using a Bruker Equinox 55 spectrophotometer. For FTIR analysis, 5 mg of solid sample was ground in an agate mortar with 30 mg of KBr and then pressed.

Solid-state NMR spectra were collected using a Varian Unity Inova spectrometer with a 9.39 T wide-bore Oxford magnet. ^{29}Si Magic Angle Spinning (MAS) experiments were performed at a 7 kHz spinning rate with a probe configured for 4 mm Si_3N_4 rotors. MAS experiments were run with a recycle time of 15 s, 2.5 μs pulse length (7.5 μs 90° pulse) that produced relaxed spectra and 50 kHz spectral window. ^{29}Si Cross Polarization Magic Angle Spinning (CPMAS) spectra were collected with contact times of 2 and 4 ms and a recycle time of 4

s. ^{13}C CPMAS spectra were collected with a recycle time of 4 s and contact time of 4 ms. ^{29}Si and ^{13}C chemical shifts were referenced to that of tetramethylsilane. The use of CPMAS provides spectra with a better signal-to-noise ratio. The CPMAS NMR spectra should be effective for proton-rich components. A poorly protonated Si atom is normally affected by slow rates of cross polarisation from the few bonded or remote protons (Mehring 1983; De Giudici et al 2009; Sanna et al. 2013).

XAS experiments were conducted at the Zn K-edge (9659 eV) at the XAFS beamline, ELETTRA, Trieste (Italy). In addition to biomineral samples, crystalline abiotic hemimorphite was analysed as reference compound. Standard procedures (see Meneghini et al. 2012; Medas et al. 2014a and b for more details) were applied for XAS raw data treatment, normalisation and extraction of structural signal EXAFS (extended X-ray absorption fine structure) $\chi(k)$ using the ESTRA programme (Meneghini et al. 2012). The normalised spectra were analysed in the near-edge (XANES: near edge X-ray absorption fine structure) and extended (EXAFS) regions (see Supplementary Materials SM, section S1, for details about XAFS data analysis).

RESULTS

Microscopy, SEM and TEM analysis

Fluorescent tracer observed with confocal microscopy imaging (Medas et al. 2012a) indicated that cyanobacterium *L. frigida* built hemimorphite-like biomineral sheaths during their life activity (Figs. 1a and b). SEM analysis revealed that the biomineral consisted of nanoparticles that precipitated both on bacterial filaments (Figs. 1c and d) and on polymeric substances secreted by bacteria (Fig. 1e). In detail, cross sections of mineralised bacterial filaments, which were investigated by low-resolution TEM (Fig. 1f), showed that these nanoparticles had a dimension ranging from few tens of nanometres to hundreds of nanometres.

FTIR analysis

The FTIR spectra of the samples WM9, WM13 and hemimorphite in the range 400–4000 cm^{-1} are shown in Fig. 2. Biomineral spectra fit well with the frequency trends of hemimorphite (Frost et al. 2007). The existence of Zn-O and Si-O bonds were confirmed, including the asymmetric stretching ν_a(Si-O) at 1048 cm^{-1}, ν_s(Si-O) at 934–

933 and 880–875 cm^{-1}, Zn-O stretching vibration at 1437–1433 cm^{-1} and Zn-O bending vibration at 455–470 cm^{-1} (Wilson 1994; da Fonseca et al. 2004). In the spectra of biomineral samples, the absence of the peak at 697 cm^{-1}, which was characteristic of crystalline hemimorphite and corresponded to the symmetric stretching vibration of Si-O bonding, further suggested that the samples presented an amorphous nature (Saikia et al. 2008; Ramasamy and Suresh 2009). This result was in agreement with the XRD patterns (Medas et al. 2014b). See SM, section S2, for additional details on FTIR analysis.

^{29}Si NMR analysis

The ^{29}Si MAS and CPMAS NMR spectra of the samples WM9 and WM13 are shown in Fig. 3. The ^{29}Si MAS NMR spectra of both samples showed signals in the range from −65 ppm to - 90 ppm. Specifically, two resolved signals at −68.3 and −76.8 ppm, a shoulder at −85 ppm and a tail in the range −90 ppm to −100 ppm were more evident in WM13 than in WM9.

The ^{29}Si chemical shifts in Zn silicates depend mainly on the degree of condensation of the silicate tetrahedra and the number of Zn atoms in the first coordination sphere of Si (Stebbins et al. 1986; Kirkpatrick 1988). Si tetrahedra, Q_n,, can share corners through oxygen bridges with n other Si atoms (n varies in the range 0–4). According to Lippmaa et al. (1980; see also Kohn 2006), increasing n corresponds to a more negative ^{29}Si NMR chemical shift. The downfield resonance observed at −68.3 ppm fell in the chemical shift range characteristic of Q_0 silicate units, whereas the signal at −76.8 ppm and the shoulder at −85 ppm fell in the chemical shift range characteristic of Q_1-type silicate units (Lippmaa et al. 1980). In particular, the peak at −76.8 ppm fell close to the chemical shift (−77.9 ppm) assigned to Q_1 silicate units of hemimorphite ($Zn_4Si_2O_7(OH)_2 \cdot nH_2O$; Lippmaa et al. 1980). This attribution was in agreement with the FTIR result.

Figure 3 also shows the ^{29}Si MAS NMR spectra obtained with cross polarisation (CPMAS) collected at a contact time of 4 ms (see SM, section S3, for details). The features of the ^{29}Si CPMAS NMR spectra of the WM9 and WM13 samples were found to correspond to silica units, which bear protons in close proximity to Si atoms.

148 Therefore, the ^{29}Si peaks observed at −68.6, −76.8 and −85 ppm were attributed to different condensation states
149 of Si tetrahedra always having neighbouring hydrogen atoms.
150

151 **^{13}C NMR analysis**

152 The CPMAS spectra of WM9 and WM13 samples collected at 1 ms contact time (Fig. 4) showed a large number
153 of broad signals. The broad signals could be attributed to the presence of organic molecules. The O-alkyl region
154 (50–110 ppm) included signals from methoxyl carbon (56 ppm), oxygen-substituted carbon, ring carbons in
155 carbohydrates, carbons in ethers (65–95 ppm) and anomeric carbon in carbohydrates (105 ppm). The aromatic
156 and substituted aromatic region (110–165 ppm) contained signals from aromatic carbon (110–145 ppm) and
157 phenolic carbon (145–160 ppm). Signals from carboxylic, amide, ester carbon and carbonyl carbon in the
158 peptide bond (160–190 ppm; Malcolm 1989) were also observed (Opella et al. 1987).

159 **XAS analysis**

160 Zn K-edge XAS data analysis was performed in the XANES and EXAFS regions, providing complementary
161 details. Comparing the XANES region with reference spectra allows understanding of the Zn coordination
162 chemistry of the samples. This technique is a powerful tool for natural materials, which are often characterised
163 by complex multi-phase composition. EXAFS data analysis provides accurate structural details, such as the
164 average coordination numbers and interatomic distances around Zn atoms.
165 Figure 5 shows the Zn K near-edge normalised XAS spectra (XANES) of biomineral samples compared with the
166 spectrum of hemimorphite reference compound. Biomineral sample spectra were all similar and depicted
167 analogies (labelled A–D) with the spectrum of the hemimorphite reference sample, particularly the splitting of
168 the white line peak A and the shape of the shoulder between A and B features. Such similarity was confirmed by
169 examining the extended region (EXAFS) of the spectra (Figs. 6a and b). The EXAFS oscillations of biomineral
170 and hemimorphite samples depicted the same frequency, but the biomineral samples showed less structured
171 oscillations likely due to the larger structural disorder. This phenomenon caused lack of next neighbour shell
172 signal, which was in accordance with the amorphous nature of the biomineral resulting from XRD analysis and

in agreement with previous findings (Medas et al 2014b). This trend was clearly recognisable in the moduli of Fourier transforms (Fig. 6b), in which the second shell features appeared definitively weaker in biomineral samples relative to the hemimorphite sample.

Medas et al. (2014b) previously suggested that the similarities between the Zn K-edge XANES spectra of the biominerals and that of hemimorphite (Fig. 5) indicate that the Zn biomineral is a low crystalline variety of this Zn silicate (bio-hemimorphite). In the previous work, EXAFS analysis demonstrated that the Zn local structure in biomineral samples is characterised by four oxygen shells at R_{ZnO} of 1.95 Å; a next neighbour shell made of Zn atoms was recognised at 3.3 Å with average multiplicity (CN) between 0.7 and 2. In this work, an additional statistically significant shell is recognised, namely, Zn-Si at 3 Å (see discussion in SM section S5 and Fig. S3).

Figures 6a and b show the k-weighted Zn EXAFS spectra $k\chi(k)$ along with the best fit curves and the Fourier Transform (FT) moduli, respectively. The quantitative results of the reference compound and biomineral samples obtained from EXAFS data refinement are reported in Table 2. According to the previous work (Medas et al. 2014b), when refining the Zn EXAFS spectra of the biomineral samples, the ZnO coordination number should be fixed at 4 (accordingly to the hemimorphite model). The other parameters were allowed to vary for each shell. Biomineral samples consistently showed (Table 1) a first Zn-O shell at 1.95 Å and a second Zn-Si shell at 3.0 Å, with coordination number varying between 0.8 and 1.3 and a disorder factor (mean square relative displacement) σ^2 between 0.008 and 0.018 $Å^2$. A third Zn-Zn shell was found at 3.3 Å with CN between 1 and 1.8 and σ^2 between 0.010 and 0.013 $Å^2$. Notably, the analysis of these data recognised the contribution of an additional coordination shell made by light elements (likely Si), with multiplicity around 1 (see SM, section S5 and Fig. S3). This finding strengthens the similarity of local atomic structure (coordination chemistry and geometry) around Zn with that of hemimorphite mineral, and it was in agreement with previous results (Medas et al. 2014b). Adding further coordination shells and multiple scattering signals did not statistically improve the best fit. The weak differences with crystalline hemimorphite were reasonably due to the highly disordered nature of this bio-hemimorphite, in which the lack of long range order was evident in XRD patterns and by the absence of next neighbour shells in the EXAFS data (Fig. 6).

199 ## DISCUSSION

200 Biosphere–geosphere interactions deeply affect the Si biogeochemical cycle. Cyanobacteria, diatoms and
201 sponges contribute a significant fraction of silica in past and actual oceans and in sedimentary environments
202 (Vrieling et al. 2003). Amorphous silica, poorly ordered clays and highly crystalline silicates, such as kaolinite
203 and glauconite-like minerals, precipitate as a result of the interactions between binding sites within the bacterial
204 cell walls and soluble metal species and silicate anions (Schultze-Lam et al. 1995; Ferris et al. 1986; Konhauser
205 et al. 1993, 1994; Ferris et al. 1987; Fortin and Beveridge 1997). Fe phyllosilicates, which belong to the smectite
206 group, can form in hydrothermal environments on the cell walls of bacteria (Fortin et al. 1998). Mg
207 phyllosilicate biosynthesis in microbialites are importance also because they represent the EPS-rich matrix
208 where Ca carbonates precipitate (Couradeau et al. 2011; Gérard et al. 2013; Zeyen et al. 2015 and references
209 therein). Silica or other tectosilicates, such as zeolites (Caldelas and Weis, 2017; Valchev et al. 2003; Ma and
210 Yamaji, 2008), and a hemimorphite-like phase (Medas et al. 2015) were found in roots and/or leaves of several
211 plant species.
212 How the silicic acid reaches its final site of deposition is still largely unknown and remains an active area of
213 study across the globe (Belton et al. 2012). Evidence for transport of Si by biochemical transporters is available
214 for three classes of studied silicified organisms (diatoms, sponges and higher plants). In this study, bio-
215 hemimorphite was investigated to gain insight into the mechanisms that cyanobacteria use to control the
216 condensation of Si tetrahedra and biomineralization. Waters of Rio Naracauli are saturated with respect to
217 hemimorphite (Saturation Index = 5.6±1.0, Podda et al. 2014) regardless of the season. Chemical parameters that
218 can affect hemimorphite precipitation, such as Zn and Si concentrations (Zn 0.13 ± 0.03 mmol and Si 0.24 ±
219 0.01 mmol) and pH (7.8 ± 0.1), do not vary significantly during the year. In contrast to the consequent
220 thermodynamic prediction, Naracauli bio-hemimorphite precipitation is a seasonal process that only occurs
221 during summer months when hydrological regime is stationary, allowing the predominance of oligotrophic
222 cyanobacteria (Podda et al. 2014). During these periods, *L. frigida* blooms in Naracauli waters and rule
223 hemimorphite formation, suggesting that formation of hemimorphite is kinetically controlled by either a template
224 or a metabolic effect (Wanty et al. 2013). In this study, fluorescent tracer studies demonstrated (Figs. 1a and b)

that cyanobacterium *L. frigida* forms hemimorphite-like biomineral sheaths during its life activity. Hereafter, we discuss the mechanism of hemimorphite biosynthesis.

Silicon coordination environment

In this work, a Zn-Si shell was recognised around 3 Å. Moreover, ^{29}Si CPMAS spectra were found to be independent of contact time at 2 and 4 ms, indicating that all the Si atoms had neighbouring hydrogen atoms. Q_1 dimers (Fig. 3) in WM biominerals resulted in two distinct ^{29}Si chemical shifts: one at −76.8 ppm that corresponded to hemimorphite standard (Lippmaa et al. 1980) and another at −85 ppm. The double peak indicated a difference in the connectivity of SiO_4 tetrahedra with neighbouring ZnO_4 tetrahedra (Lippmaa et al. 1980; Kohn 2004) and was attributed to Si_2O_7 dimers affected by some distortion. Thus, we interpreted that protonated Si_2O_7 dimers predominated in the Si coordination of our biogenic Zn silicate. In most studies on biogenic silica (Belton et al. 2012; Zeyen et al. 2015), the apparent condensation state was higher than that observed for Zn silicate in this study. However, there is little or no evidence for occurrences of biosynthesised nesosilicates. Sahai and Tossel (2001) reported that a low condensation state may be favoured by Si organic complexation. The observed ^{29}Si shift at −85 ppm, characteristic of Q_1-type silicate units, was close to the chemical shift assigned to different organic Si complexes (Table 2). Identifying the specific organic molecules listed in Table 2 among WM samples is challenging and needs additional work. We interpreted the observed ^{29}Si shift at −85 ppm as a possible effect of biologically controlled transport of Si. The activity of Si organic complex(es) could be attributed to either template or metabolic effect.

Organic matrix and biomineral formation

On the basis of NMR sensitivity and Loss on Ignition (LOI) data (see Table S1), the amount of organic matter in bio-hemimorphite samples roughly corresponded to at least several units percent in weight. As the NMR sensitivity was around 1%, the amount of organic matter roughly varied from 1% in weight to a maximum of 10%–13% based on LOI values. ^{13}C NMR analysis revealed that carboxyl carbons and N-carboxyl carbons (carboxylic, amide and ester carbon) were the main organic species present in the organic template of the WM

250 samples. These species could be attributed to a wide range of biopolymers, such as exopolysaccharides and cell
251 wall polysaccharides, recognised in *L. frigida* by Piro et al. (2005) (see also Podda et al. 2014). Alternatively,
252 carboxyl carbons and N-carboxyl carbons could be attributed to other categories of biopolymers such as silaffins
253 (Kröger et al. 2000; Sumper et al. 2005; Wendy 2015) and amides, which can be used for silica transport during
254 biomineralization of diatoms and cyanobacteria (Incharoensakdi et al. 2010).
255 The capability of organisms to make minerals depends on the macromolecular species comprised in the organic
256 matrix; moreover, the specific macromolecular composition determines the position in three dimensions of ions
257 (Mann 1983, 2001; Addadi et al. 1987; Aizenberg et al. 1999; Mann et al. 2000; Weiss et al. 2000; Weiner and
258 Dove 2003; Gilbert et al. 2005; Sanna et al. 2015). According to Beveridge and Murray (1980), carboxyl groups
259 of the organic matrix deprotonate under the observed pH conditions (pH 7.8 ± 0.1). Deprotonation leads to a
260 negatively charged bacterial surface. Thus, biochemical conditions favour electrostatic interactions between the
261 deprotonated surface sites on the biopolymers, which are often (exo)polysaccharides, and aqueous ions
262 (Beveridge and Murray 1980, Fein et al. 1997; Fortin et al. 1998), such as Zn^{2+}, as follows:

$$R - COO^- + M^{m+} \leftrightarrow R - COO(M)^{(m-1)+}$$

263 where R is the deprotonated surface of the bacterium. Naracauli waters are always saturated with respect to
264 hemimorphite (Podda et al. 2014). Therefore, deprotonation occurring due to metabolic functions had no
265 apparent effect on pH bulk chemistry. However, Zn^{2+} ions accumulate at the biopolymer surface, reaching higher
266 concentrations than in the surrounding bulk phase. Thus, deprotonation and Zn accumulation at the biopolymer
267 surface could be the microscopic processes leading to hemimorphite formation.
268 Waters in contact with *L. frigida* biofilm are undersaturated with respect to SiO_{2am} (saturation index with respect
269 to SiO_{2am} ranging from −0.89 to −0.76). Experimental results (Yee et al. 2003) showed that the interaction
270 between Si and cell surface functional groups is weak in solutions undersaturated with respect to amorphous
271 silica (SiO_{2am}), and minimal Si sorption onto cyanobacterial surfaces occurs. Under the observed chemical
272 condition (slightly alkaline pH, undersaturation with respect to SiO_{2am}), Si is stable in solution in the form of a
273 neutrally charged complex $H_4SiO_4^0$ (Belton et al. 2012). Consequently, silicic acid may be adsorbed with the
274 condensation between the silanol group (Si–OH) of dissolved silicic acid and positively charged Zn (Fortin et al.

1998) by forming a metal ion bridge. This bridge may lead to the formation of $Si_2O_7H_6$ dimers, and their stabilisation may result in short-range-ordered domains with a hemimorphite-like structure (see Table 1).

IMPLICATIONS

The problem of silica condensation during biomineralization has been long debated. Previous studies often assumed the saturation of bulk fluid with respect to silica as the driving force for silica condensation. Carboxyl groups, components of many biopolymers, silaffins and complex biopolymers are involved in silica biomineralisation (Kröger et al. 2000; Grachev et al. 2005; Trembath-Reichert et al. 2015). The observed capability of *L. frigida* to control silica polymerisation provides pivotal insight into the understanding of strategies for silicate biomineralization mediated by bacteria in chemical conditions where the bulk fluid is undersaturated with respect to silica.

During silica biomineralization, Ostwald ripening processes are likely to occur and eventually produce phases that can have a long lifetime in rocks and sediments (Belton et al. 2012). However, the amorphous and low condensation of silica biominerals whose particles are enveloped by organic molecules can undergo recrystallisation into more stable phases (Meldrun and Cölfen, 2007). Medas et al. (2017) conducted laboratory experiments and observed that Naracauli bio-hemimorphite undergoes a rapid aging process in which morphological and structural features, after two years of interaction with water, are overprinted due to Ostwald ripening process. Thus, the observed low crystallinity and presence of organic molecules can have implications on the reactivity and solubility of the biomineral, as well as the persistency of Si_2O_7 dimers over time. The structural factors (i.e. size of low crystalline/amorphous domains, surface energy, bond length, stability of the carboxylic *glue*) that control the reactivity of bio-hemimorphite remain unclear. Further studies are needed to shed light on the kinetics of bio-hemimorphite recrystallisation and its implications on biomineral persistency over geological time.

ACKNOWLEDGEMENT

This work was granted by CERIC 2015–2020, CERIC 2016–2061 (Elettra Spa), RAS/FBS (grant number: F72F16003080002) and CESA project (number E58C16000080003). We acknowledge Prof. Pierfranco Lattanzi for his useful suggestions. Handling of AE, Alejandro Fernandez-Martinez, was greatly appreciated. The constructive suggestions of Karim Benzerara and two other reviewers are acknowledged.

REFERENCES CITED

Addadi, L., Moradian, J., Shay, E., Maroudas, N.G., and Weiner, S. (1987) A chemical model for the cooperation of sulfates and carboxylates in calcite crystal nucleation: relevance to biomineralization. Proceedings of the National Academy of Sciences U S A, 84, 2732–2736.

Aizenberg, J., Black, A.J., and Whitesides, G.M. (1999) Oriented Growth of Calcite Controlled by Self-Assembled Monolayers of Functionalized Alkanethiols Supported on Gold and Silver. Journal of the American Chemical Society, 121, 4500–4509.

Belton, D.J., Deschaume, O., and Perry, C.C. (2012) An overview of the fundamentals of the chemistry of silica with relevance to biosilicification and technological advances. The FEBS Journal, 279, 1710–1720.

Benning, L.G., Phoenix, V., and Mountain, B.W. (2005) Biosilicification: the role of cyanobacteria in silica sinter deposition. In M.G. Gadd, T.K. Semple, M.H. Lappin-Scott, Eds., Micro-organisms and Earth Systems: Advances in Geomicrobiology, p. 131–150. Society for General Microbiology Symposia. Cambridge: Cambridge University Press.

Beveridge, T.J., and Murray, RGE. (1980) Sites of metal deposition in the cell wall of Bacillus subtilis. Journal of Bacteriology, 141, 876–887.

Burne, R.V., Moore,L.S., Christy, A.G., Troitzsch, U., King, P.L., Carnerup,. M., et al. (2014). Stevensite in the modern thrombolites of Lake Clifton, Western Australia: a missing link in microbialite mineralization? Geology 42, 575–578.

Caldelas, C., and Weiss, D.J. (2017) Zinc Homeostasis and isotopic fractionation in plants: a review. Plant Soil, 411, 17–46.

Couradeau, E., Benzerara, K., Moreira, D., Gérard, E., Ka´zmierczak, J., Tavera, R., et al. (2011). Prokaryotic and Eukaryotic community structure in field and cultured microbialites from the alkaline lake Alchichica (Mexico) ed.J.A. Gilbert. PLoSONE, 6, 1-12.

da Fonseca, M.G., da Silva Filho, E.C., Machado, R.S.A. Jr., Arakaki, L.N.H., Espinola, J.G.P., and Airoldi, C. (2004) Zinc Phyllosilicates Containing Amino Pendant Groups. Journal of Solid State Chemistry, 177, 2316–2322.

De Giudici, G., Podda, F., Sanna, R., Musu, E., Tombolini, R., Cannas, C., Musinu, A., and Casu, M. (2009) Structural properties of biologically controlled hydrozincite: a HR-TEM and NMR spectroscopic study. American Mineralogist, 94, 1698–1706.

De Giudici, G., Lattanzi, P., Medas D. (2014a). Synchrotron Radiation & Environmental Sciences. In S. Mobilio et al., Eds., Synchrotron Radiation, Springer-Verlag Berlin Heidelberg, pp. 661-676.

De Giudici, G., Wanty, R.B., Podda, F., Kimball, B.A., Verplanck, P.L., Lattanzi, P., Cidu, R., Medas D. (2014b). Quantifying Biomineralization of Zinc in the Rio Naracauli (Sardinia, Italy), Using a Tracer Injection and Synoptic Sampling. Chemical Geology, 384, 110–119.

De Giudici, G., Medas, D., Meneghini, C., Casu, M.A., Gianoncelli, A., Iadecola, A., Podda, S., and Lattanzi, P. (2015) Microscopic biomineralization processes and Zn bioavailability: a synchrotron-based investigation of Pistacia lentiscus L. roots. Environmental Science and Pollution Research, 22, 19352–61.

Drum, R.W., and Pankratz, H.S. (1964). Post mitotic fine structure of Gomphonema parvulum. Journal of Ultrastructure Research, 10, 217–223.

Fein, J.B., Daughney, C.J., Yee, N., and Davis, T.A. (1997) A chemical equilibrium model for metal adsorption onto bacterial surfaces. Geochimica et Cosmochimica Acta, 61, 3319–3328.

Fein, J.B., Scott, S., and Rivera, N. (2002) The effect of Fe on Si adsorption by Bacillus subtilis cell walls: insights into non-metabolic bacterial precipitation of silicate minerals. Chemical Geology, 182, 265–273.

Ferris, F.G., Beveridge, T.J., and Fyfe, W.S. (1986) Iron-silica crystallite nucleation by bacteria in a geothermal sediment. Nature, 320, 609–611.

345 Ferris, F.G., Fyfe, W.S., and Beveridge, T.J. (1987) Bacteria as nucleation sites for authigenic minerals in a metal
346 contaminated lake sediment. Chemical Geology, 63, 225–232.

347 Fortin, D. and Beveridge, T.J. (1997) Role of the bacterium, Thiobacillus, in the formation of silicates in acidic mine
348 tailings. Chemical Geology, 141, 235–250.

349 Fortin, D., Grant Ferris, F., and Scott, S.D. (1998) Formation of Fe-silicates and Fe-oxides on bacterial surfaces in samples
350 collected near hydrothermal vents on the Southern Explorer Ridge in the Northeast Pacific Ocean. American Mineralogist,
351 83, 1399–1408.

352 Frost, R.L., Bouzaid, J.M., and Reddy, B.J. (2007) Vibrational spectroscopy of the sorosilicate mineral hemimorphite
353 $Zn_4(OH)_2Si_2O_7 \cdot H_2O$. Polyhedron, 26, 2405–2412.

354 Gérard, E., Ménez, B., Couradeau, E., Moreira, D., Benzerara, K., Tavera, R., et al. (2013). Specific carbonate–microbe
355 interactions in the modern microbialites of Lake Alchichica (Mexico). The ISME Journal. 7,1997–2009.

356 Gilbert, P.U.P.A., Abrecht, M., and Frazer, B.H. (2005) The Organic-Mineral Interface in Biominerals. In J.F. Banfield,
357 K.H. Nealson, J. Cervini-Silva, Eds., Molecular Geomicrobiology, 59, p. 157–185. Reviews in Mineralogy and
358 Geochemistry, Mineralogical Society of America, Washington D.C.

359 Kirkpatrick, R.J. (1988) MAS NMR spectroscopy of minerals and glasses. F.C. Hawthorne, Ed., Spectroscopic methods in
360 mineralogy and geology, 18, p. 358–359. Reviews in Mineralogy, Washington D.C.

361 Köhler, B., Singer, A., and Stoffers, R. (1994) Biogenic nontronite from marine white smoker chimneys. Clays Clay
362 Minerals, 42, 689–701.

363 Kohn, S.C. (2004) NMR studies of silicates glasses. EMU Notes in Mineralogy, 6, 399–419.

364 Kohn, S.C. (2006) Structural studies of OH in nominally anhydrous mineral using NMR. Reviews in Mineralogy and
365 Geochemistry, 62, 53–62.

366 Konhauser, K.O. (1998) Diversity in bacterial iron mineralization. Earth Science Review, 43, 91–121.

Konhauser (2016) Geomicrobial Interactions with Silicon. In H.L. Ehrlich, A. Kappler, D.K. Newmann, Eds., Geomicrobiology, p. 237–255, CRC Press, Taylor & Francis Group, NW.

Konhauser, K.O., Fyfe, W.S., Ferris, F.G., and Beveridge, T.J. (1993) Metal sorption and mineral precipitation by bacteria in two Amazonian river systems: Rio Solimões and Rio Negro, Brazil. Geology, 21, 1103–1106.

Konhauser, K.O., Scultze-Lam, S., Ferris, F.G., Fyfe, W.S., Longstaff, F.J., and Beveridge, T.J. (1994) Mineral precipitaiton by epilithic biofilms in the Speed river, Ontario, Canada. Applied and Environmental Microbiology, 60, 549–553.

Kröger, N., Deutzmann, N., Bergsdorf, C., and Sumper M. (2000). Species-specific polyamines from diatoms control silica morphology. Proceedings of the National Academy of Science. 97, 14133–14138

Incharoensakdi, A., Jantaro, S., Raksajit, W., Mäenpää, P. (2010). Polyamines in cyanobacteria: biosynthesis, transport and abiotic stress response. Current Research, Technology and Education Topics in Applied Microbiology and Microbial Biotechnology. Microbiology Book Series-Ed Mendez-Vilas A. - Number 2. 23-32.

Lippmaa, E., Mägi, M., Samoson, A., Engelhardt, G., and Grimmer, A.R. (1980) Structural studies of silicates by solid-state high-resolution silicon-29 NMR. Journal of the American Chemical Society, 102, 4889–4893.

Ma, J.F., Miyak, Y., and Takahashi, E. (2001) Silicon as a beneficial element for crop plants. In L.E. Datnoff, G.H. Snyder, G.H. Korndoerfer, Eds., Silicon in Agriculture, 8, p. 17–39, Elsevier Science, Amsterdam.

Ma, J.F., and Yamaji, N. (2008) Functions and transport of silicon in plants. Cellular and Molecular Life Sciences, 19, 3049–57.

Malcolm, R.L. (1989) Application of solid state ^{13}C NMR spectroscopy to geochemical studies of humic substances, In M.H.B. Hayes, P. MacCarthy, R.L. Malcom, and Swift R.S., Eds., Humic Substances 2: In search of structure, p. 339–372, Wiley, New York.

Mann, S. (1983) Mineralization in biological systems. Structure and Bonding, 54, 125–174.

389 Mann, S. (2001) Biomineralization: Principles and Concepts in Bioinorganic Materials Chemistry, 17, 210 p., Oxford
390 University Press, Oxford.

391 Mann, K., Weiss, I.M., Andre, S., Gabius, H.J., and Fritz, M. (2000) The amino-acid sequence of the abalone (*Haliotis*
392 *laevigata*) nacre protein perlucin. European Journal of Biochemistry, 267, 5257–5264

393 Medas D., Cidu R., Lattanzi P., Podda F. and De Giudici G. (2012a) Natural biomineralization in the contaminated
394 sediment-water system at the ingurtosu abandoned mine. In Bio-Geo Interactions in Metal-Contaminated Soils (eds. E.
395 Kothe and A. Varma), Soil Biology, vol. 31, Springer-Verlag, Berlin. pp. 113–130.

396 Medas, D., Cidu, R., Lattanzi, P., Podda, F., Wanty, R.B. and De Giudici, G. (2012b) Hydrozincite seasonal precipitation at
397 Naracauli (Sardinia–Italy): hydrochemical factors and morphological features of the biomineralization process, Applied
398 Geochemistry, 27, 1814–1820.

399 Medas, D., De Giudici, G., Podda, F., Meneghini, C., and Lattanzi, P. (2014a) Apparent energy of hydrated biomineral
400 surface and apparent solubility constant: an investigation of hydrozincite, Geochimica Cosmochimica Acta 140, 349–364.

401 Medas, D., Lattanzi, P., Podda, F., Meneghini, C., Trapananti, A., Sprocati, A.R., Casu, M.A., Musu, E., and De Giudici, G.
402 (2014b) The amorphous Zn biomineralization at Naracauli stream, Sardinia: electron microscopy and X-ray absorption
403 spectroscopy. Environmental Science and Pollution Research, 21, 6775–6782.

404 Medas, D., De Giudici, G., Casu, M.A., Musu, E., Gianoncelli, A., Iadecola, A., Meneghini, C., Tamburini, E., Sprocati,
405 A.R., Turnau, K., and Lattanzi, P. (2015) Microscopic Processes Ruling the Bioavailability of Zn to Roots of *Euphorbia*
406 *pithyusa* L. Pioneer Plant. Environmental Science and Technology, 49, 1400–1408.

407 Medas, D., Podda, F., Meneghini, C., and De Giudici, G. (2017) Stability of biological and inorganic hemimorphite:
408 Implications for hemimorphite precipitation in non-sulfide Zn deposits. Ore Geology Reviews, 89, 808–821.

409 Mehring, M. (1983) Principles of High Resolution NMR in Solids, 2nd ed., 342 p. Springer-Verlag, New York.

410 Meldrum, F. and Cölfen, H. (2007) Controlling mineral morphologies and structures in biological and synthetic systems.
411 Chemical Reviews, 108, 4332–4432.

412 Meneghini, C., Bardelli, F., and Mobilio, S. (2012) ESTRA-FitEXA: a software package for EXAFS data analysis. Nuclear
413 Instruments and Methods in Physics Research Section B, 285, 153–157.

414 Neumann, D., and zur Nieden, U. (2001) Silicon and heavy metal tolerance of higher plants. Phytochemistry, 56, 685–692.

415 Opella SJ, Stewart PL, Valentine KG. (1987) Structural analysis of solid-state NMR measurement of peptides and
416 proteins. Quarterly Reviews of Biophysics,19, 7–49

417 Phoenix, V.R., Adams, D.G., and Konhauser, K.O. (2000) Cyanobacterial viability during hydrothermal biomineralization.
418 Chemical Geology, 169, 329–338.

419 Piro, G., Congedo, C., Leucci, M.R., Lenucci, M., and Dalessandro, G. (2005) The biosynthesis of exo- and cell wall-
420 polysaccharides is sensitive to brefeldin A in the cyanobacterium Leptolyngbya VRUC 135. Plant Biosystems, 139, 107–
421 112.

422 Podda, F., Medas, D., De Giudici, G., Ryszka, P., Wolowski, K., and Turnau, K. (2014) Zn biomineralization processes and
423 microbial biofilm in a metal-rich stream (Naracauli, Sardinia). Environmental Science and Pollution Research, 21, 6793–
424 6808.

425 Ramasamy, V., and Suresh, G. (2009) Mineral Characterization and Crystalline Nature of Quartz in Ponnaiyar River
426 Sediments, Tamilnadu, India. American-Eurasian. Journal of Scientific Research, 4, 103–107.

427 Sahai, N., and Tossel, J.A. (2001) Formation energies and NMR chemical shifts calculated for putative serine-silicate
428 complexes in silica biomineralization. Geochimica et Cosmochimica Acta, 65, 2043–2053.

429 Sahai, N. (2004) Calculation of ^{29}Si NMR shifts of silicate complexes with carbohydrates, amino acids, and
430 MuHicarboxylic acids: Potential role in biological silica utilization. Geochimica et Cosmochimica Acta, 68, 227–237.

431 Saikia, B.J., Parthasarathy, G., and Sarmah, N.C. (2008) Fourier transform infrared spectroscopic estimation of crystallinity
432 in SiO_2 based rocks. Bulletin of Materials Science, 31, 775–779.

433 Sanna, R., De Giudici, G., Scorciapino, A.M., Floris, C., Casu, M. (2013) Investigation of the hydrozincite structure by
434 infrared and solid-state NMR spectroscopy. American Mineralogist, 98, 1219–1226.

435 Sanna, R., Medas, D., Podda, F., Meneghini, C., Casu, M., Lattanzi, P., Scorciapino, M.A., Floris, C., Cannas, C., and De
436 Giudici, G. (2015) Binding of bis-(2-ethylhexil) phthalate at the surface of hydrozincite nanocrystals: an example of organic
437 molecules absorption onto nanocrystalline minerals. Journal of Colloid & Interface Science, 1, 298–306.

438 Schaller, J., Brackhage, C., Bäucker, E., and Dudel, E.G. (2013) UV-screening of grasses by plant silica layer. Journal of
439 Biosciences, 38, 413–416.

440 Schultze-Lam, S., Ferris, F.G., Konhauser, K.O., and Wiese, R.G. (1995) In situ silicification of an Icelandic hot spring
441 microbial mat: implications for microfossil formation. Canadian Journal of Earth Sciences, 32, 2021–2026.

442 Simpson, T.L. (1984) The Cell Biology of Sponges. Springer, New York.

443 Stebbins, J.F., Murdoch, J.B., Carmichael, I.S.E., and Pines, A. (1986) Defects and Short-range Order in Nepheline Group
444 Minerals: a Silicon-29 Nuclear Magnetic Resonance Study. Physics and Chemistry of Minerals, 13, 371–381.

445 Sumper, M., Brunnerb, E., Lehmann, G., (2005) Biomineralization in diatoms: Characterization of novel polyamines
446 associated with silica. Federation of European Biochemical Societies Letters, 579, 3765–3769.

447 Trembath-Reicherta, E., Paul Wilson, J., McGlynna, S.E., Fischer, W.W. (2015). Four hundred million years of
448 silica biomineralization in land plants. Proceedings National Academy of Science, 112, 5449–5454

449 Urrutia, M.M., and Beveridge, T.J. (1993). Mechanism of Silicate Binding to the Bacterial Cell Wall in Bacillus subtilis.
450 Journal of Bacteriology, 175, 1936–1945.

451 Valtchev, V., Smaihi, M., Faust, A.C., and Vidal, L. (2003) Biomineral-silica-induced zeolitization of *Equisetum arvense*.
452 Angewandte Chemie International Edition, 42, 2782–2785.

453 Vrieling, E.G. Hazelaar, S., Gieskes, W.W.C., Sun, Q., Beelen, T.P.M., and van Santen, R.A. (2003) Silicon
454 biomineralization: towards mimicking biogenic silica formation in diatoms. In W.E.G. Müller, Ed., Progress in Molecular
455 and Subcellular Biology, 33, p. 301–334, Springer Berlin Heidelberg.

456 Wanty, R.B., De Giudici, G., Onnis, P., Rutherford, D., Kimball, B.A., Podda, F., Cidu, R., Lattanzi, P., and Medas, D.
457 (2013) Formation of a low-crystalline Zn-silicate in a stream in SW Sardinia, Italy. Proceedings of the Fourteenth
458 International Symposium on Water-Rock Interaction. Procedia Earth and Planetary Science, 7, 888–891.

459 Weiner, S., and Dove, P.M. (2003) An overview of biomineralization processes and the problem of the vital effect. Reviews
460 in Mineralogy and Geochemistry, 54,1–29.

461 Weiss, I.M., Kaufmann, S., Mann, K., and Fritz, M. (2000) Purifi cation and characterization of perlucin and perlustrin, two
462 new proteins from the shell of the mollusk haliotis laevigata. Biochemical and Biophysical Research Communications, 267,
463 17–21.

464 Wendy J. S. (2015) Solid-state NMR studies of proteins immobilized on inorganic surfaces. Solid State Nucl Magn Reson.
465 70, 1–14.

466 Wilson, M.J. (1994) Clay Mineralogy Spectroscopic and Chemical Determinative Methods, (1st ed.), Chapman & Hall,
467 London.

468 Yee, N., Phoenix, V.R., Konhauser, K.O., Benning, L.G., and Ferris, F.G. (2003) The effect of cyanobacteria on silica
469 precipitation at neutral pH: implications for bacterial silicification in geothermal hot springs. Chemical Geology, 199, 83–
470 90.

471 Zeyen, N., Benzerara, K., Li, J., Groleau, A., Balan, E., Robert, J.L., Esteve, I., Tavera, R., Moreira, D., Lopez-Garcia, P.
472 (2015). Formation of low-T hydrated silicates in modern microbialites from Mexico and implications for microbial
473 fossilization. Frontiers in Earth Science, 3, 10.3389/feart.2015.00064.

474

475
476

477

478

479

Figure 1. Microscopic features. (a) and (b): Confocal microscopy images and fluorescence marker (Medas et al., 2012, modified). Red is for cyanobacteria, whereas blue is for Zn matrix. (c) to (f): SEM and TEM images of WM samples. Nanoparticles of the biomineral on bacterial filaments (c and d) and on the polymeric substances secreted by bacteria (e) observed by SEM; nanoparticles around the bacterial filaments observed in cross sections by low-resolution TEM (f).

Figure 2. FTIR spectra of WM9 and WM13 hemimorphite and hydrozincite samples (a and b). The enlargement at the bottom (a) better shows the region 1800-400 cm^{-1}.

Figure 3. ^{29}Si MAS and $^{29}Si/1H$ CPMAS spectra of WM9 and WM13 samples. The dotted line marks the position of the crystalline hemimorphite band (−77.9 from Lipmaa et al. 1980).

Figure 4. ^{13}C CPMAS NMR spectra of WM9 and WM13 samples.

Figure 5. Normalised Zn K-edge absorption spectra (near edge region) of hemimorphite and biomineral samples, which were vertically shifted for the sake of clarity. The main features of hemimorphite spectra (A to D) can also be recognised in the biomineral sample, suggesting an analogous local structure.

Figure 6. Experimental data (points) and best fits (full lines) (a) and Fourier Transforms (b) of EXAFS spectra of hemimorphite (Hemim) and biomineral samples (WM9-WM23), which were vertically shifted for the sake of clarity.

Table 1. Mean values and standard deviations of the fit parameters for EXAFS analysis of hemimorphite and biomineral samples.

	CN	R (Å)	σ^2(x10^{3}Å)	ΔE (eV)	R^2
WM9				4.7(6)	0.01
ZnO	4*	1.94(1)	5.4(3)		
ZnSi	1.3(1)	2.94(2)	18(2)		

ZnZn	1.8(2)	3.30(2)	13(2)		
WM13				5.5(5)	0.01
ZnO	4*	1.95(1)	6.0(3)		
ZnSi	1.0(1)	2.99(2)	13(2)		
ZnZn	1.3(1)	3.32(2)	11(2)		
WM20				5.0(5)	0.01
ZnO	4*	1.95(1)	6.6(3)		
ZnSi	0.8(1)	3.03(2)	8.2(2)		
ZnZn	1.0(1)	3.33(2)	10(2)		
WM23				5.7(7)	0.01
ZnO	4*	1.95(1)	6.4(5)		
ZnSi	0.9(1)	3.00(2)	12(2)		
ZnZn	1.3(1)	3.32(2)	11(3)		
Hemim					
ZnO	4.0(4)	1.93(2)	4.1(6)	4.12(5)	0.01
ZnSi	3.1(5)	3.24(3)	8.3(8)		
ZnZn	4.1(6)	3.40(3)	10(1)		

CN = coordination number; R = interatomic distance; σ^2 = Debye-Waller; R^2 = best fit factor; ΔE = edge energy shift. CN* for the first shell in the biomineral samples was fixed to 4. The number in brackets indicates the uncertainty on the last digit of the refined parameters.

557 **Table 2. ^{29}Si chemical shift for selected organic Si complexes.**

Organic Si complex	Chemical shift (ppm)	Reference
$(CH_3)_3SiCH(CH_3)Cl$	−84.17	Scholl et al., 1972
$(C_2H_5)_3Si(n\text{-}C_4H_9)$	−85.41	Scholl et al., 1972
$(CH_2COOC_2H_5)(CH_3)Si(C_2H_5)_2$	−85.6	Scholl et al., 1972
$(CH_3)_2(CH(CH_3)Cl)SiC_2H_5$	−86.02	Scholl et al., 1972
$(C_2H_5)_3Si(s\text{-}C_4H_9)$	−86.66	Scholl et al., 1972
$C_3H_7F_3OSSi$	−86.4	Pestunovich et al., 1985
$C_{25}H_{23}NO_4Si$	−87	Tacke et al., 1991
$(C_3H_6O_3)_2Si$	≈ −85[a]	Sahai, 2004

[a]data from graphic (Fig. 1 in Sahai, 2004).

558

Figure 1

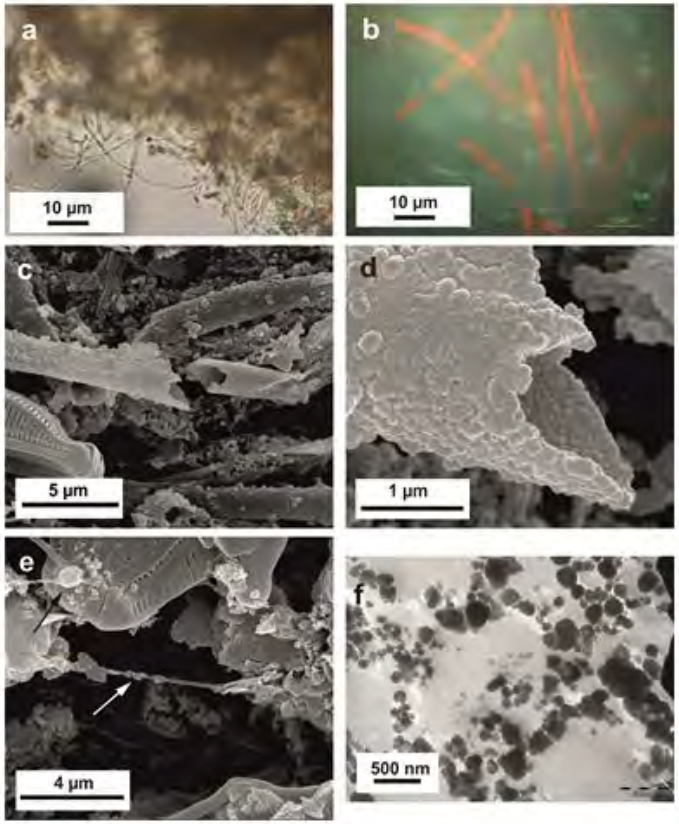

Figure 2

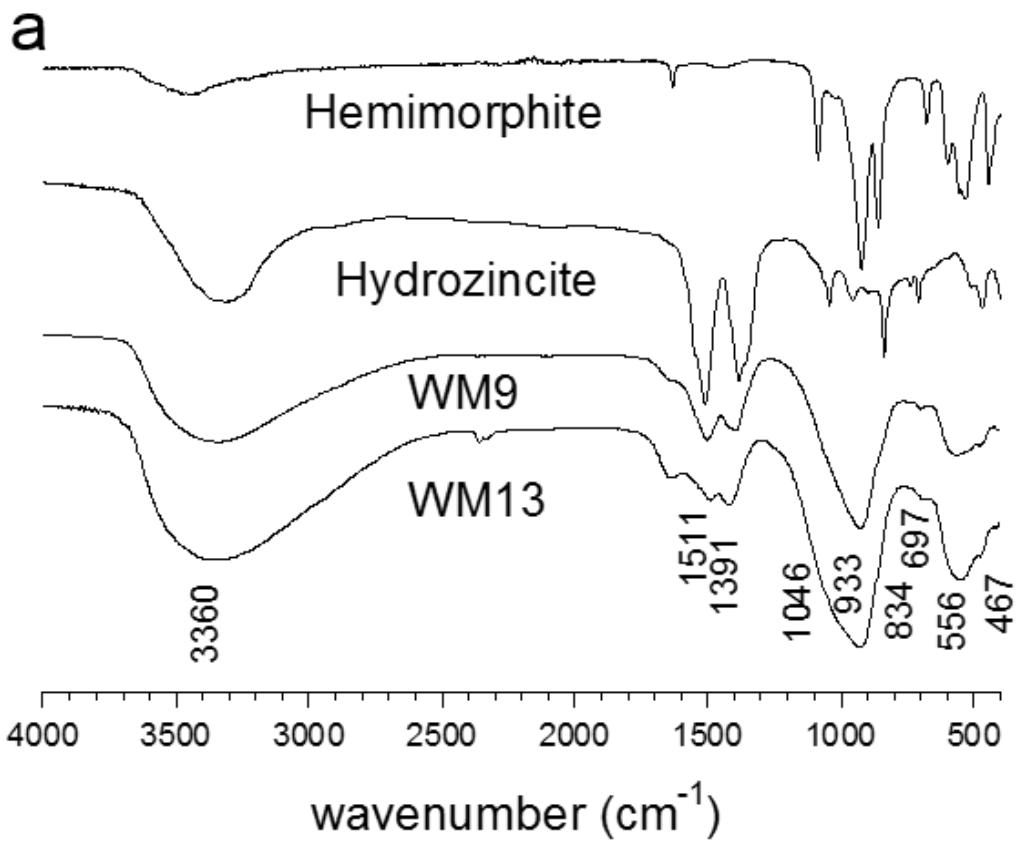
a
Hemimorphite
Hydrozincite
WM9
WM13
3360
1511
1391
1046
933
834
697
556
467
4000
3500
3000
2500
2000
1500
1000
500
wavenumber (cm-1)

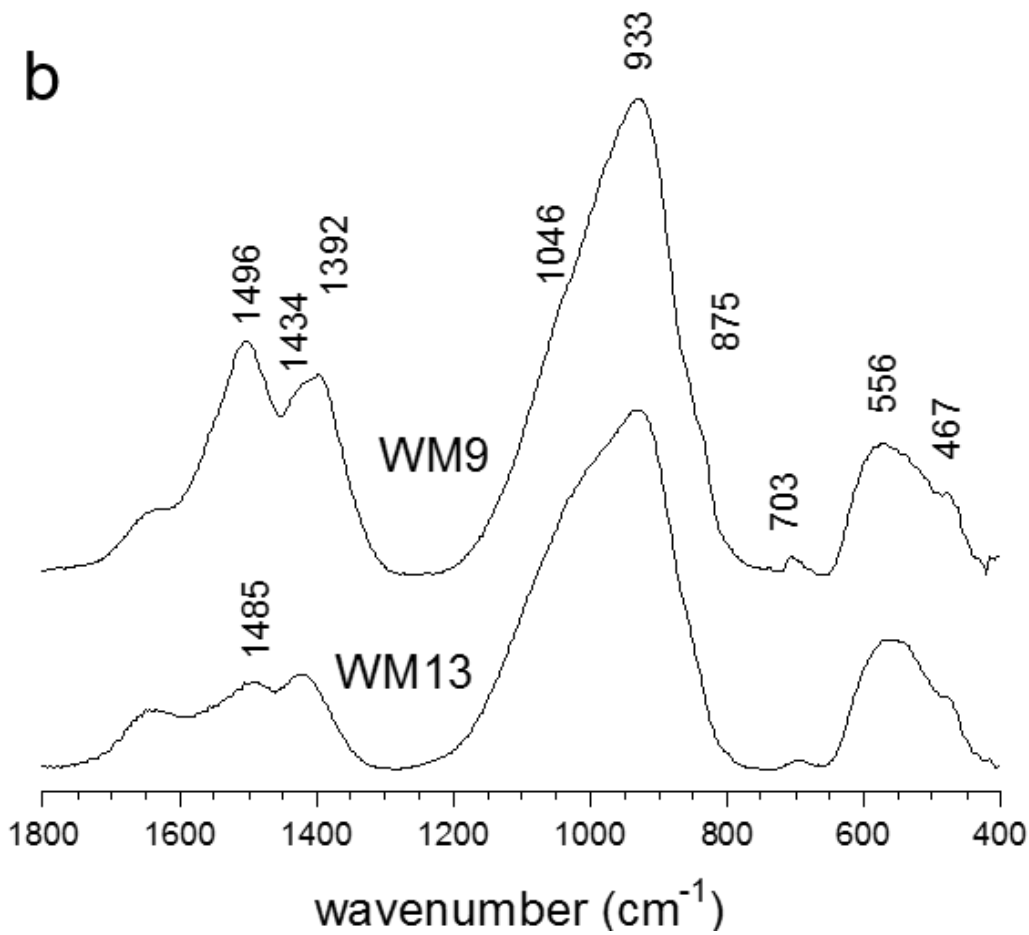
b
933
1496
1434
1392
1046
875
556
467
703
WM9
1485
WM13
1800
1600
1400
1200
1000
800
600
400
wavenumber (cm-1)

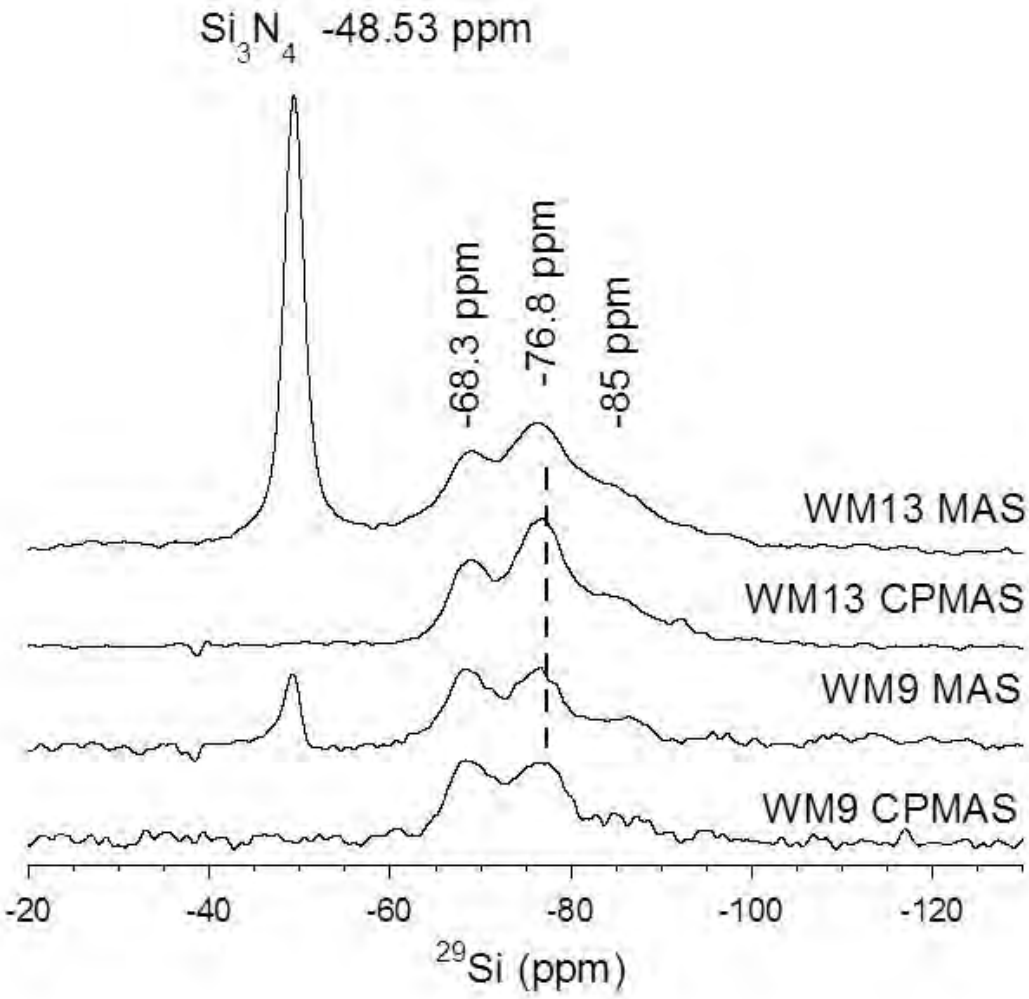
Si3N4 -48.53 ppm
-68.3 ppm
-76.8 ppm
-85 ppm
WM13 MAS
WM13 CPMAS
WM9 MAS
WM9 CPMAS
-20
-40
-60
-80
-100
-120
29Si (ppm)

Figure 4

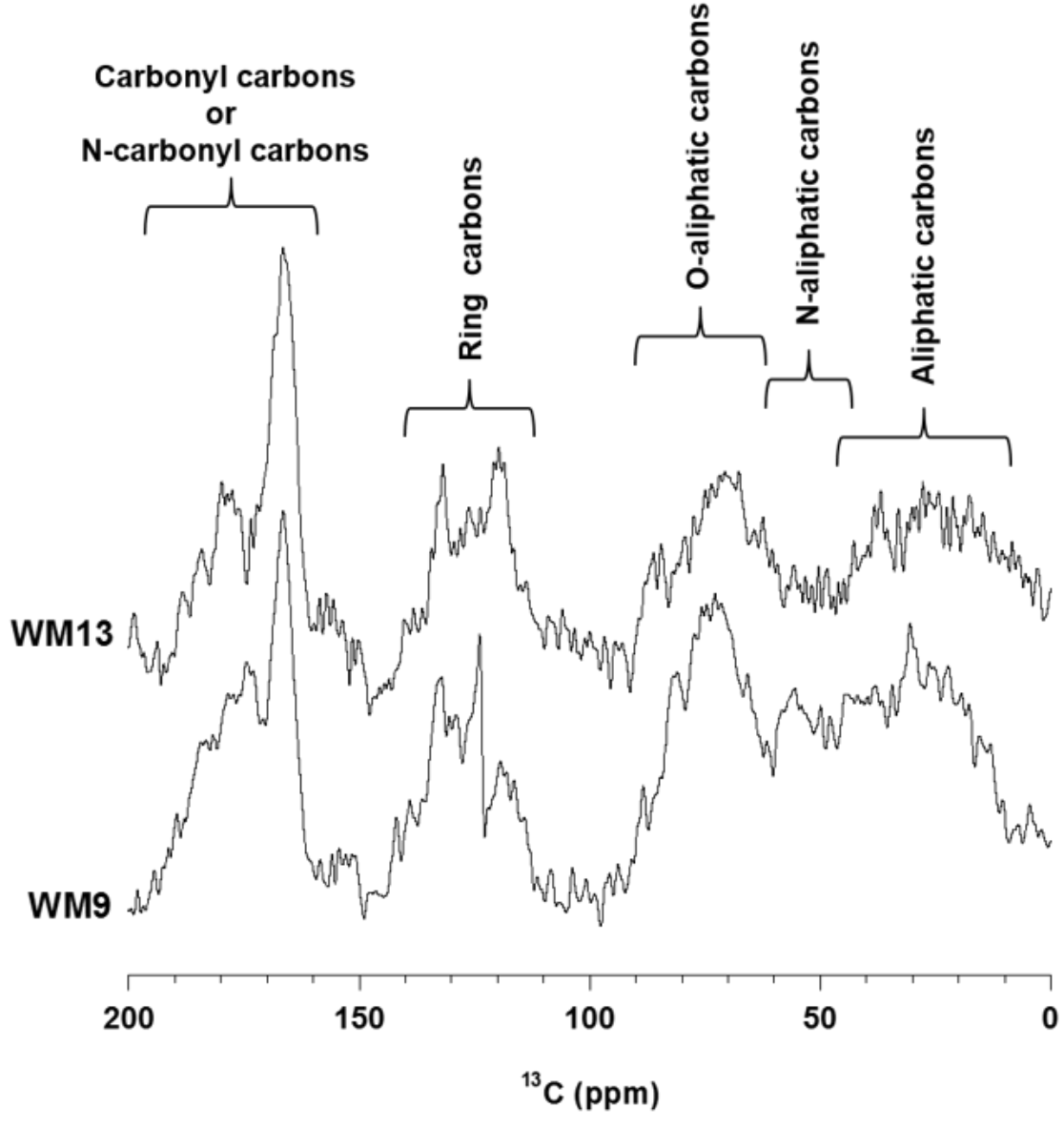
Carbonyl carbons
or
N-carbonyl carbons
Ring carbons
O-aliphatic carbons
N-aliphatic carbons
Aliphatic carbons
WM13
WM9
200
150
100
50
0
13C (ppm)

Figure 5

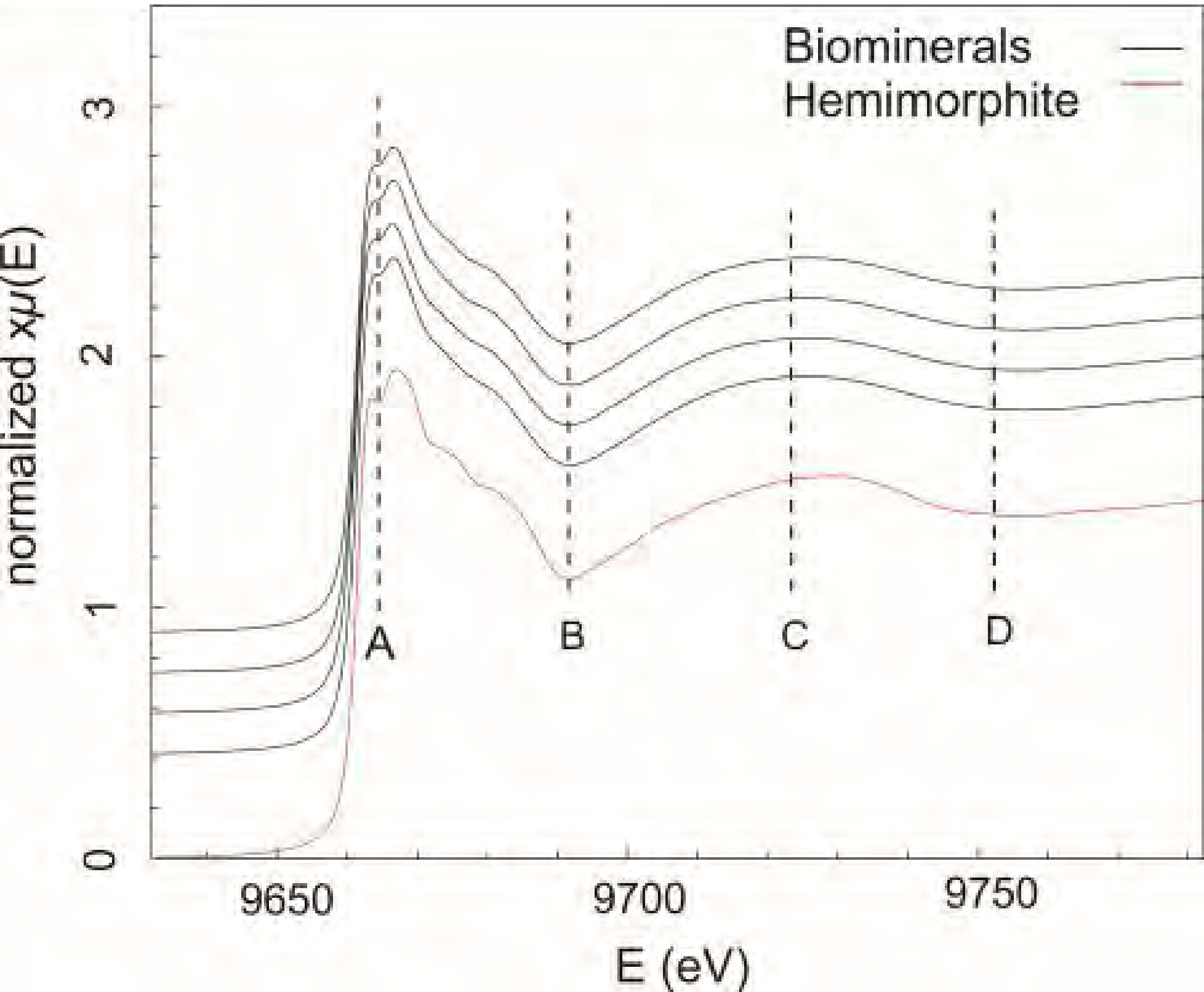
Biominerals
Hemimorphite
normalized xμ(E)
0
1
2
3
A
B
C
D
9650
9700
9750
E (eV)

Figure 6

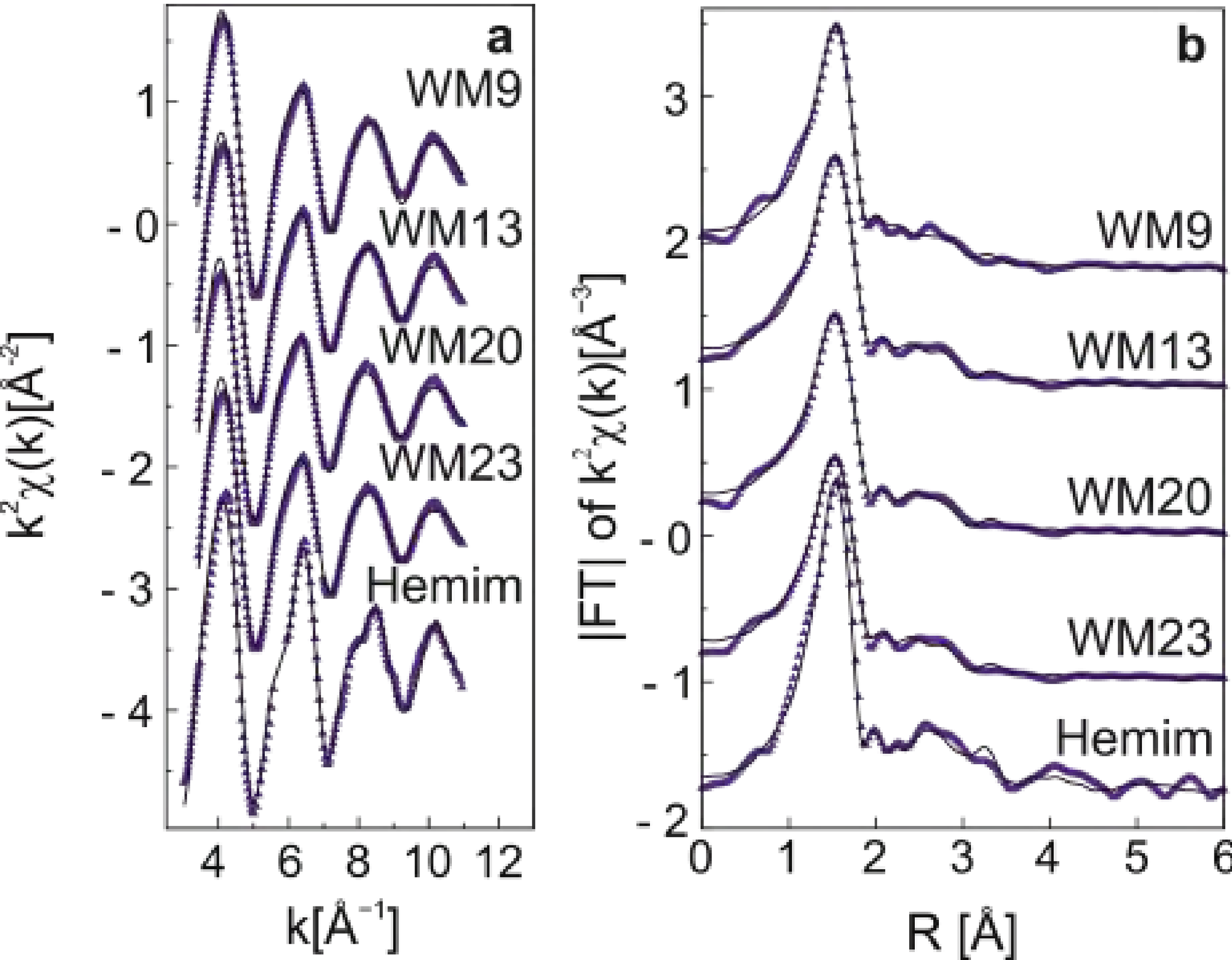
a
WM9
WM13
WM20
WM23
Hemim
1
- 0
- 1
- 2
- 3
- 4
4
6
8
10
12
k[Å⁻¹]
k²χ(k)[Å⁻²]
b
WM9
WM13
WM20
WM23
Hemim
3
2
1
- 0
- 1
- 2
0
1
2
3
4
5
6
R [Å]
|FT| of k²χ(k)[Å⁻³]